Impact of cross-saturation in sensorless control of transverse-laminated synchronous reluctance motors

Impact of Cross-Saturation in Sensorless Control of Transverse-Laminated Synchronous Reluctance Motors

Paolo Guglielmi, Michele Pastorelli, *Member, IEEE*, and Alfredo Vagati, *Fellow, IEEE*

***Abstract*—Synchronous reluctance (SyR) motors are well suited to a zero-speed sensorless control, because of their inherently salient behavior. However, the cross-saturation effect can lead to large errors on the position estimate, which is based on the differential anisotropy. These errors are quantified in the paper, as a function of the working point. The so-calculated errors are then found in good accordance with the purposely obtained experimental measurements. The impact of the amplitude of the carrier voltage is then pointed out, leading to a mixed (carrier injection plus electromotive force estimation) control scheme. Last, a scheme of this type is used, with a commercial transverse-laminated SyR motor. The robustness against cross-saturation is shown, in practice, and the obtained drive performance is pointed out proving to be effective for a general-purpose application.**

***Index Terms*—Cross-saturation effect, sensorless ac drives, sensorless control, synchronous reluctance (SyR) motor.**

I. Introduction

THE MANY advantages of sensorless ac drives are nowadays well recognized. The lower cost, the reduced motor size, the elimination of a sensor cabling, and the increased reliability are extending sensorless technology to a wider and wider class of practical applications.

Although the methods based on the fundamental excitation of the machine [e.g., generated back electromotive force (EMF)] are still appropriate for specific drive applications, the interest has been focused in the last decade to those methods that are suitable for very low and zero speed. This extends the sensorless technology to various types of low-resolution position control, as well as to those cases of speed control where an extremely high accuracy is wanted (e.g., in the textile industry).

The methods suited to position control are generally based on the deterministic spatial saliencies and require some kind of a persistent excitation, at least at a low speed [23], [24]. Many kinds of excitation are proposed, in the literature, including various types of carrier signals and modified pulsewidth-modulation (PWM) [1], [6], [11], and [15] patterns. Rotating vectors [2], [17], [18] are adopted as well as stationary (pulsating) vectors [12], [13], [22], and common mode signals too [21]. Both voltage [2], [13], [17], [18], [22] and current [12], [16] are used, as injected signals.

Manuscript received August 8, 2004; revised December 27, 2004. Abstract published on the Internet January 25, 2006.

The authors are with the Dipartimento di Ingegneria Elettrica, Politecnico di Torino, Turin 10129, Italy (e-mail: paolo.guglielmi@polito.it; michele.pastorelli@polito.it; alfredo.vagati@polito.it).

Digital Object Identifier 10.1109/TIE.2006.870716

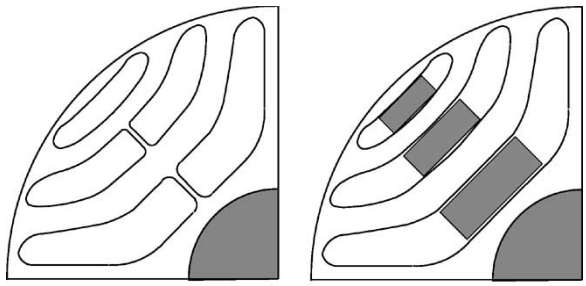

Fig. 1. Schematic of (a) TLSyR rotor and (b) PMASR rotor.

On the other hand, the availability of a position signal and the need for a deterministic saliency can shift the attention from induction motors to motors of the synchronous type naturally exhibiting a salient behavior, i.e., synchronous reluctance (SyR) and interior permanent-magnet (IPM) motors.

In fact, the zero-speed sensorless control of induction motors can require purposely engineered saliencies, like those described in [23]. The effect of rotor slots can also be used at that aim [15], [18], although this effect is strongly reduced by a rotor skewing. On the contrary, IPM and SyR motors are inherently salient and do not require any design modification, in general. Moreover, they show a better efficiency, as known. Thus, a larger use of these motors is expected in the next future, for sensorless applications.

In particular, the SyR motor would be the best suited to general-purpose sensorless drives, because of its inherent low cost, at least if the transverse-laminated design is adopted [9], [20]. On the other hand, the flux–current magnetic relationship of the transverse-laminated synchronous reluctance (TLSyR) motor is highly nonlinear [19] and the commonly used sensorless control schemes cannot be uncritically adopted, without taking into account the above told peculiarity. Of course, the same is true for the permanent-magnet-assisted synchronous reluctance (PMASR) motor, whose magnetic characteristics are very similar [25]. In Fig. 1, the schematic rotor cross sections are shown of (a) a TLSyR motor and of (b) a PMASR motor. As seen, the rotor laminae are strictly similar, apart from some quantity of added permanent-magnet (PM) material.

Anyway, in the following, the attention is focused on the TLSyR motor for simplicity. The magnetic peculiarities of TLSyR motors are pointed out and discussed, while their impact on a sensorless-control performance is evidenced, both

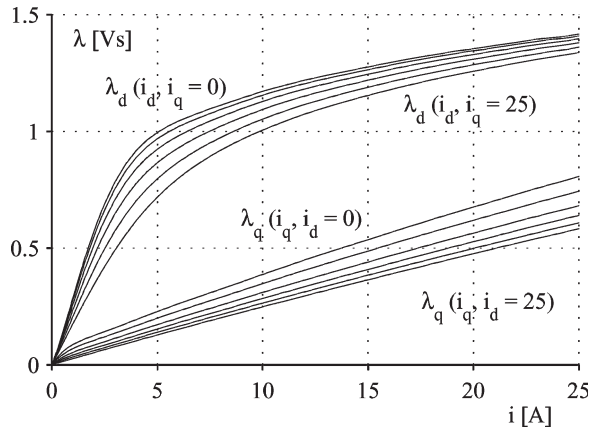

Fig. 2. Flux–current relationship of a commercial TLSyR motor.

by analysis and experimental tests. Moreover, a control scheme is illustrated, which is robust against the cross-saturation and the effective drive performance is shown through experimental verification.

II. Differential Magnetic Behavior and Sensorless Orientation Error

The flux–current characteristics of a commercial TLSyR motor (EARP, Italy) are shown in Fig. 2. They have been accurately measured, as illustrated in a previous paper [19]. The d-axis is taken in the direction of maximum permeance. Both i_d, i_q currents are varied from 0 to 25 A, while the rated motor current is about 10 A (peak).

From the figure, the nonlinear magnetic behavior of both fluxes is well evidenced. Of course, the saturation effect is more evident on the d-axis, but the relevant effect of cross-saturation can be pointed out, for both axes.

As far as zero-speed sensorless control is concerned, a linearized magnetic modeling has to be taken into account. In fact, whatever kind of exciting signal is used, the position information is found from the differential anisotropy exhibited by the motor in the actual working point, e.g., in the (i_d, i_q) plane.

The general flux–current equations are written in (1), where the needed transversality condition is evidenced [19]. From (1), the linearized model (2) is obtained. Of course, the differential inductances l_d, l_q, l_{dq} heavily depend on the chosen working point. Note that the symbols $\delta\lambda_{dq}\delta i_{dq}$ have been used to indicate small-signal flux and current vectors, as well as column matrices in (2). The cross-saturation effect is represented by the l_{dq} term, whose sign changes according to motoring or braking action. This is explained since the flux amplitude on one axis is always reduced by the current on the other axis, whatever its sign is. Thus, l_{dq} is negative when i_d, i_q have the same sign and positive in the opposite case

$$\begin{cases} \lambda_d = \lambda_d(i_d, i_q) \\ \lambda_q = \lambda_q(i_d, i_q) \end{cases} \qquad \frac{\partial \lambda_d}{\partial i_q} = \frac{\partial \lambda_q}{\partial i_d} = l_{dq} \tag{1}$$

$$\delta\lambda_{dq} = \begin{vmatrix} l_d & l_{dq} \\ l_{dq} & l_q \end{vmatrix} \delta i_{dq} \qquad l_{dq}\mathrm{sgn}(i_d i_q) < 0. \tag{2}$$

By using the complex notation and introducing the complex-conjugate current $\delta i'_{dq} = \delta i_d - j\delta i_q$, (2) can be rewritten as (3), where the forward and backward components are evidenced. As can be seen, the backward coefficient becomes complex, due to the cross-saturation term l_{dq}. As a consequence, the backward component is rotated by the ε angle (4), leading to an error in detecting the rotor position.

$$\delta\lambda_{dq} = \frac{l_d + l_q}{2}\delta i_{dq} + \left(\frac{l_d - l_q}{2} + j l_{dq}\right)\delta i'_{dq} \tag{3}$$

$$\varepsilon = \mathrm{arctg}\frac{2l_{dq}}{l_d - l_q}. \tag{4}$$

Equation (3) gives the small-signal flux vector when the small-signal current vector is imposed, as is the case of [12]. However, since a voltage signal is more commonly injected, reference is made to (5), which represents the inverse relationship of (3). Of course, the backward component of (5) is still rotated by the same ε angle given by (4).

$$\delta i_{dq} = \frac{l_d + l_q}{2\Delta}\delta\lambda_{dq} - \left(\frac{l_d - l_q}{2\Delta} + j\frac{l_{dq}}{\Delta}\right)\delta\lambda'_{dq}$$
$$\Delta = l_d l_q - l_{dq}^2. \tag{5}$$

In the literature [23], (5) is more commonly written on stationary axes. If a stationary (α, β) reference is considered, the relationships (6) hold, where ϑ is the (electrical) angle between the synchronous and stationary frames. After substitution, (7) is obtained.

$$\delta i_{dq} = e^{-j\vartheta}\delta i_{\alpha\beta} \quad \delta\lambda_{dq} = e^{-j\vartheta}\delta\lambda_{\alpha\beta} \quad \delta\lambda'_{dq} = e^{j\vartheta}\delta\lambda'_{\alpha\beta} \tag{6}$$

$$\delta i_{\alpha\beta} = \frac{l_d + l_q}{2\Delta}\cdot\delta\lambda_{\alpha\beta} - \left(\frac{l_d - l_q}{2\Delta} + j\frac{l_{dq}}{\Delta}\right)e^{2j\vartheta}\cdot\delta\lambda'_{\alpha\beta}. \tag{7}$$

It is a common choice in the literature to apply a small-signal rotating voltage, at a carrier pulsation ω_c. Thus, (8) are valid and (9) is obtained, which represents the most common form of this equation. The small signal amplitudes have been indicated as δv, $\delta\lambda$, and δi. Also, the complex backward coefficient has been split into amplitude and argument, owing to (4)

$$\begin{aligned} \delta v_{\alpha\beta} &= \delta v \cdot e^{j\left(\omega_c t + \frac{\pi}{2}\right)} \\ \delta\lambda_{\alpha\beta} &\cong \frac{\delta v}{\omega_c} e^{j\omega_c t} \\ \delta\lambda'_{\alpha\beta} &\cong \frac{\delta v}{\omega_c} e^{-j\omega_c t} \end{aligned} \tag{8}$$

$$\begin{aligned} \delta i_{\alpha\beta} = &\left[\frac{l_d + l_q}{2\Delta}\cdot\frac{\delta v}{\omega_c}\right]e^{j\omega_c t} + \\ &- \frac{\delta v}{\omega_c}\left[\sqrt{\left(\frac{l_d - l_q}{2\Delta}\right)^2 + \left(\frac{l_{dq}}{\Delta}\right)^2}\right] \\ &\cdot e^{j(2\vartheta + \varepsilon - \omega_c t)}, \qquad \text{for } l_d > l_q. \end{aligned} \tag{9}$$

To detect the ϑ angle, the negative sequence signal is obtained through a proper filtering and its phase is tracked, since it contains the wanted information. However, (9) shows that the

cross-saturation introduces on ϑ, an error equal to $\varepsilon/2$, since the angle $(2\vartheta + \varepsilon)$ is effectively tracked.

A similar situation occurs when a sinusoidal pulsating signal is injected instead of the rotating one. If a sinusoidal voltage (flux) is injected, the corresponding sinusoidal current is detected and the situation is tracked for which both $\delta\lambda_{dq}$ and δi_{dq} vectors have the same direction. This can be imposed from (5), by substituting (10). Thus, (11) is obtained, where amplitude and argument of the backward coefficient have been evidenced, as already done in (9)

$$\delta i_{dq} = \delta i e^{j\psi} \quad \delta\lambda_{dq} = \delta\lambda e^{j\psi} \quad \delta\lambda'_{dq} = \delta\lambda e^{-j\psi} \tag{10}$$

$$\frac{\delta i}{\delta\lambda} = \frac{l_d + l_q}{2\Delta} - \left[\sqrt{\left(\frac{l_d - l_q}{2\Delta}\right)^2 + \left(\frac{l_{dq}}{\Delta}\right)^2}\right] \cdot e^{j\varepsilon} \cdot e^{-2j\psi}, \qquad \text{for } l_d > l_q. \tag{11}$$

As seen, (11) can be satisfied for $\psi = (\varepsilon/2) \pm k(\pi/2)$ where k is any positive integer. Of course, the d-axis is generally tracked, because of the lower $\delta i/\delta\lambda$ ratio.

From the above discussion, it can then be concluded that the cross-saturation introduces an error equal to $\varepsilon/2$ in the ϑ detection, irrespectively of the rotating or pulsating injected sinusoidal signals. To evaluate the impact of this phenomenon, reference is made to the TLSyR motor whose flux–current characteristics are reported in Fig. 2.

From these characteristics, the behavior of the differential inductances l_d, l_q, and l_{dq} can be calculated, owing to the interpolation model presented in [19]. These inductances are much variable, depending on the working point, as it is shown in Fig. 3, where the curves are plotted corresponding to the boundary points of the considered area in the (i_d, i_q) plane (both i_d, i_q span from 0 to 25 A).

It can be seen that both l_d and l_q are larger than $|l_{dq}|$, while l_d can be lower than l_q, when the d-flux path is brought to saturation. Let us also point out that $l_d(i_d, i_q)$ is an even function of both i_d and i_q variables, and the same holds for $l_q(i_d, i_q)$. On the contrary, $l_{dq}(i_d, i_q)$ is an odd function of both i_d, i_q variables, as already told. When l_d becomes lower than l_q, the real part of the backward coefficient in (7) changes its sign. In fact, the injected signal now sees the larger permeance in the q-direction and the argument of the backward component for $t = 0$ would exhibit a jump π wide, at least if ϑ is still measured from the usual axis and disregarding cross-saturation. However, the angle ε has a jump too, for $l_d = l_q$, since the denominator of (4) changes its sign. As a consequence, the argument of the backward component for $t = 0$ does not show any jump, since the cross-saturation effect exactly compensates for the inverse-anisotropy phenomenon. Of course, when l_{dq} changes its sign, the error sign changes too, accordingly with (4). In conclusion, the error due to cross-saturation on the ϑ estimate is given by (12). The sign of l_{dq} is opposite to $\mathrm{sgn}\,(i_d i_q)$ and to the sign of the torque.

In Fig. 4, the absolute value of the error (12) is plotted with reference to the first quadrant, as a function of the argument γ

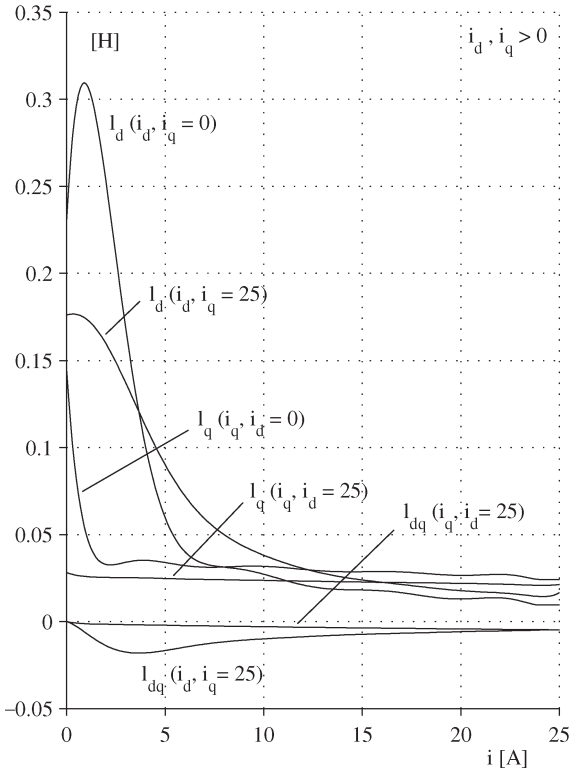

Fig. 3. l_d, l_q, and l_{dq} on the boundary of the considered squared area in the first quadrant (25 A wide).

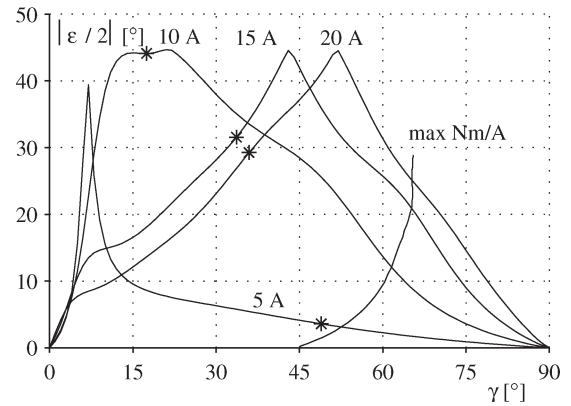

Fig. 4. Absolute value of the error (12), as a function of γ for various i amplitudes, where $\gamma = \angle\, i_{dq}$ (rated current 10 A).

of the current vector i_{dq}, for some given values of the current amplitude i

$$\mathrm{err} = -\frac{1}{2}|\varepsilon|\mathrm{sgn}(i_d i_q). \tag{12}$$

As can be seen, the error can reach 45° for near rated or overcurrent values, when the argument γ is smaller than that corresponding to the maximum N·m/A curve. However, for practical γ values, at rated current, a maximum error of 13° is pointed out. It might then be concluded that the impact of this error is limited, in practice. On the contrary, when sensorless operation occurs, the set γ^* and real γ values are different from each other, since the current control is based on the wrong reference. Thus, the effective working point moves from e.g.,

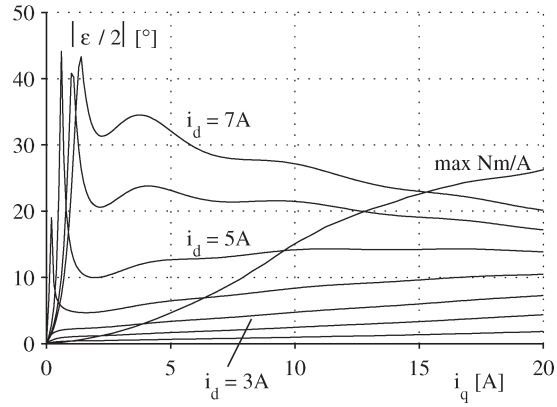

Fig. 5. Absolute value of the error as a function of i_q for $i_d = 1, 2, 3, \ldots 7$ A.

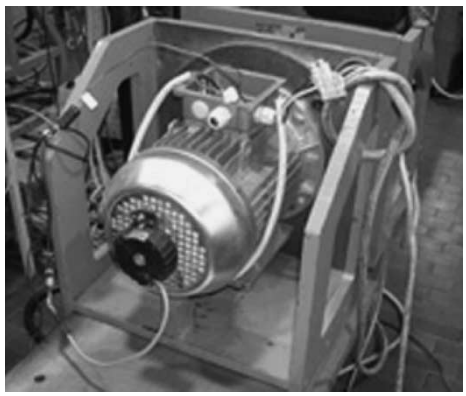

Fig. 6. Tested general-purpose TLSyR motor.

the maximum N·m/A curve towards the lower γ values, since $\gamma - \text{err}(\gamma, i) = \gamma^*$. As a consequence, much larger errors can be experienced than expected for $\gamma = \gamma^*$.

Still with reference to Fig. 4, the stars show some sensorless errors (γ, i), while the corresponding set points (γ^*, i) are chosen on the maximum N·m/A locus. As seen, an error of about 45° occurs at $i = 10$ A, while the corresponding ϑ error with $\gamma = \gamma^*$ is near to 13°. As a consequence, the sensorless operation can become critical, even for a near-rated current value.

On the other hand, there are also problems at no-load, as it is shown by Fig. 5. In this figure, the error is plotted as a function of i_q current, for some set values of i_d current.

As seen, even for near-rated values of i_d (e.g., 4 or 5 A), at light load (low i_q) very large errors are present. If a limited error is wanted at light load, the i_d current has to be reduced, as suggested from the figure, where the maximum N·m/A curve is still shown.

Anyway, the d-flux cannot be reduced too much, because, in this case, a loose of synchronism could occur, for any disturbance. Thus, a minimum λ_d (or i_d) value must be set, when adopting a maximum N·m/A strategy, at a low speed. The choice of this value must then be traded off with the related error, in case of the sensorless control. On the other hand, at high speed the flux value is dictated by a voltage limitation: however, in this case, a different sensorless strategy is opportune, as shown in the following.

III. Experimental Validation

To verify the predicted impact of the cross-saturation on a sensorless control, some experimental tests have been performed. The general-purpose TLSyR motor has been used (Fig. 6), whose characteristics are shown in Fig. 2.

The motor is 18 N·m rated, self-cooled like general-purpose induction motors are. During the tests, the motor was driven by a coaxial, speed-controlled drive. A low speed was chosen (100 r/min), to simplify the filtering matter.

The four-pole TLSyR motor under a test was current controlled and the i_d, i_q values were freely imposed. In addition, a rotating-voltage vector was applied, at a 400-Hz carrier frequency. The resulting current signal was measured and its negative sequence (backward) component was tracked to find out the $(2\tilde{\vartheta} + \varepsilon)$ angle estimate, as suggested by (9). Then,

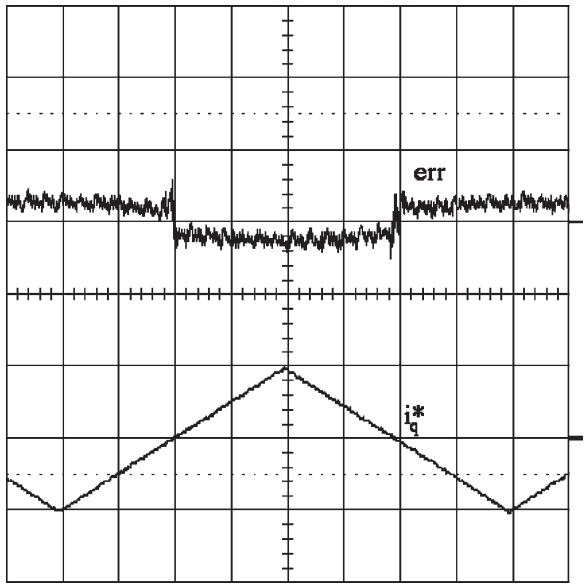

Fig. 7. Measured error for $i_d = 3$ A and i_q varied from -20 to $+20$ A. Measured error: err (25° el/div), set motor current: i_q^* (20 A/div). Time base 1 s/div.

the error $(\tilde{\vartheta} - \vartheta)$ was measured, with ϑ coming from a shaft encoder.

In Figs. 7 and 8, the measured error is shown, to be compared with that calculated from (12) and plotted in Fig. 5. Fig. 7 refers to $i_d = 3$ A, while Fig. 8 is obtained with $i_d = 7$ A. In both figures, the i_q current is varied linearly from -20 to $+20$ A, as shown. The accordance between measured and calculated results is very good. In Fig. 8, the peak error of nearly 45° can be evidenced, when i_q is in the proximity of zero (near to 2 A), as predicted by Fig. 5.

Let us observe that during the tests of Figs. 7 and 8, the applied (rotating) voltage vector was quite large, that is 125 V. This corresponds, at 400 Hz, to a rotating flux vector whose amplitude is 0.05 Vs. This was done to get reliable estimates for all the working points, as it will be pointed out in the following.

One can then conclude that the cross saturation has an effective, important impact on the sensorless estimation of the rotor angle.

Another effect of the highly nonlinear magnetic behavior of the TLSyR machine regards the much variable differential

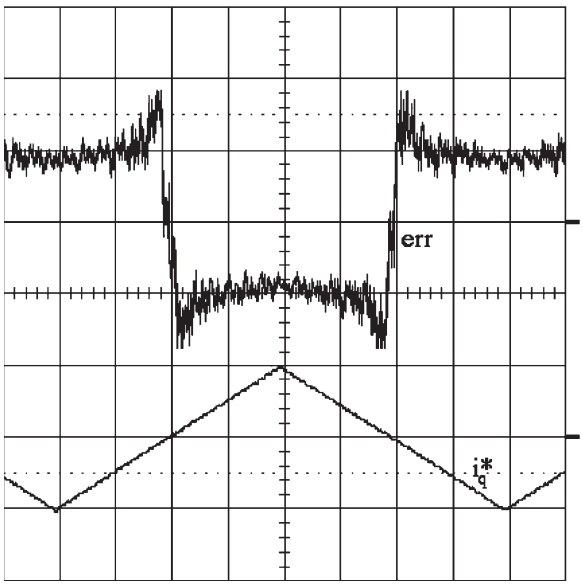

Fig. 8. Measured error for $i_d = 7$ A and i_q varied from -20 to $+20$ A. Measured error: err (25° el/div), set motor current: i_q^* (20 A/div). Time base 1 s/div.

anisotropy, and the consequent much variable amplitude of the generated negative-sequence component. With reference to (7) and to an injected flux (voltage) signal, the ratio b/f between negative and positive sequence amplitudes can be written (13). The corresponding equivalent anisotropy ratio ar is given by (14)

$$\frac{b}{f} = \frac{\sqrt{(l_d - l_q)^2 + 4l_{dq}^2}}{l_d + l_q} \tag{13}$$

$$\text{ar} = \frac{1 + \frac{b}{f}}{1 - \frac{b}{f}}. \tag{14}$$

This ratio heavily depends on the (i_d, i_q) working point, as shown by Fig. 9, where various ar = constant loci are shown, in the (i_d, i_q) plane. As seen, there are points near to d-axis where the equivalent anisotropy ratio (14) practically vanishes, making it difficult to identify the rotor position.

At the aim of verifying Fig. 9 calculations, the same experimental setup already used with Figs. 7 and 8 has been adopted. The amplitude of the injected 400-Hz rotating voltage has been varied from 0 to 300 V, when the motor was running at a fixed motor speed (100 r/min). The sinus of twice the estimated angle $\tilde{\vartheta}$ is shown, to be compared with the measured one, for different working points in the (i_d, i_q) plane. The result is reported in Figs. 10–14. Of course, when the carrier voltage amplitude is zero, no information is obtained and the sin $2\tilde{\vartheta}$ signal is corrupted by noise. The noise vanishes as the voltage is increased, in a way that is different for the various working points. In addition, a filtered sin $2\tilde{\vartheta}$ signal is given too. A simple tracking loop was used, as a filter. Of course, the tracking fails when the information is insufficient.

Let us observe that no particular care was taken in maximizing the signal-to-noise ratio. In particular, the effect of the inverter's dead time and delays was not compensated at

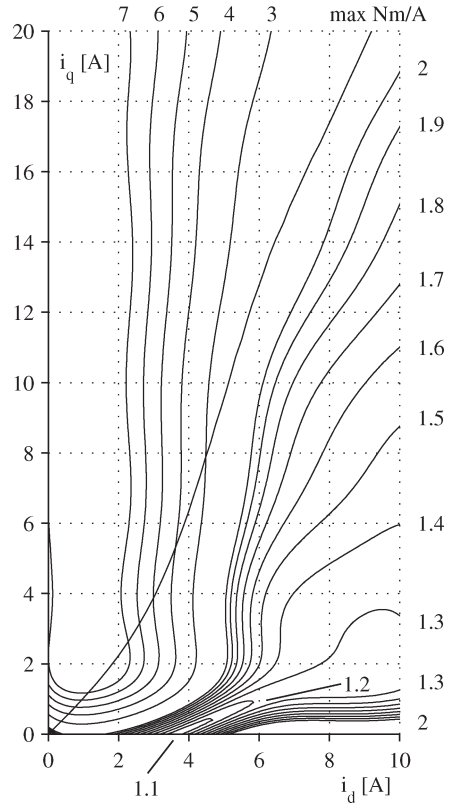

Fig. 9. Constant equivalent anisotropy ratio (ar) in the i_d, i_q plane.

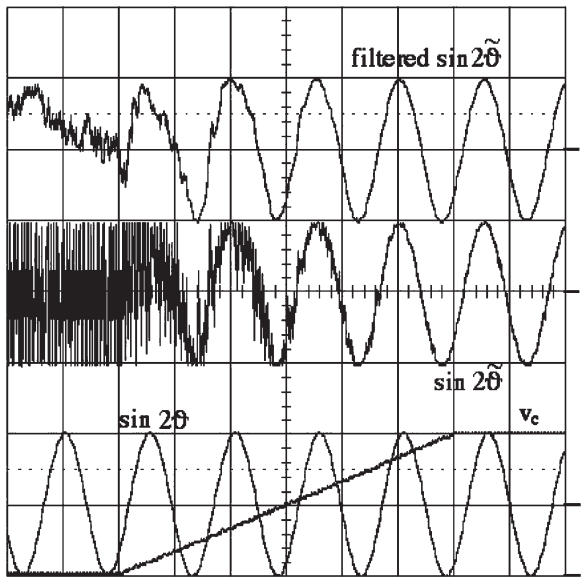

Fig. 10. Estimated angle $(\sin 2\tilde{\vartheta})$ for an injected carrier voltage v_c increased from 0 to 300 V ($i_d = i_q = 0$). Exciting (rotating) voltage: v_c (150 V/div). Time base: 100 ms/div.

all. This has been done for simplicity, since the actual goal was the experimental verification of the sensitivity of the angle estimation to the motor working points (Fig. 9).

Coming to results, Fig. 10 shows the behavior of the unexcited motor ($i_d = i_q = 0$). Because of the low anisotropy, the sin $2\tilde{\vartheta}$ signal is corrupted, until large voltage values are reached. The situation looks even worse in Fig. 11, where the point

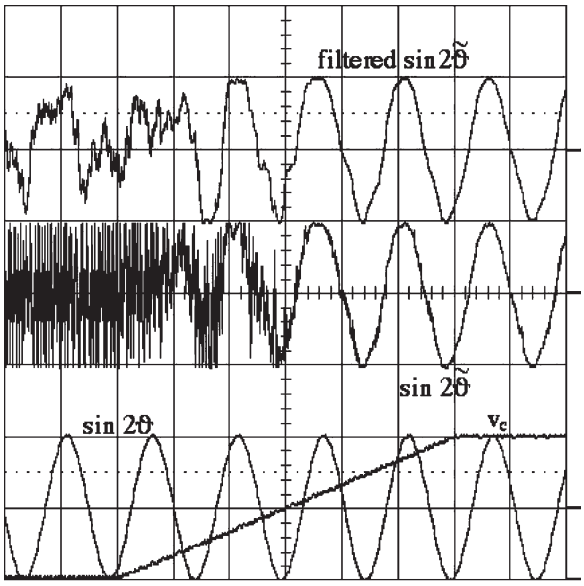

Fig. 11. Estimated angle $(\sin 2\tilde{\vartheta})$ for an injected carrier voltage v_c increased from 0 to 300 V ($i_d = 4$ A, $i_q = 0$). Exciting (rotating) voltage: v_c (150 V/div). Time base: 100 ms/div.

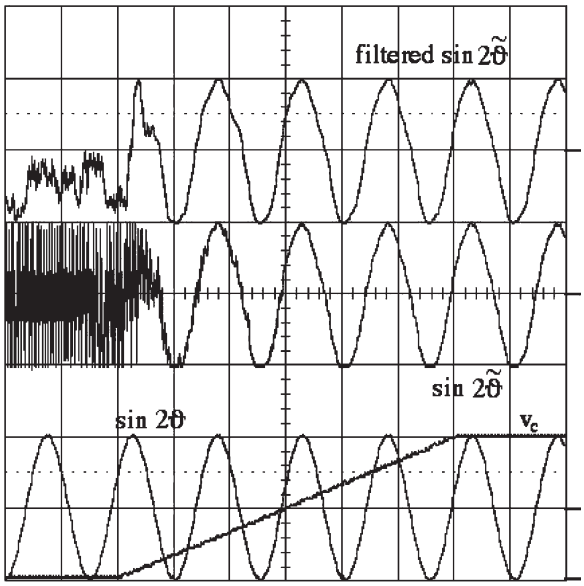

Fig. 12. Estimated angle $(\sin 2\tilde{\vartheta})$ for an injected carrier voltage v_c increased from 0 to 300 V ($i_d = 4$ A, $i_q = 2$ A). Exciting (rotating) voltage: v_c (150 V/div). Time base: 100 ms/div.

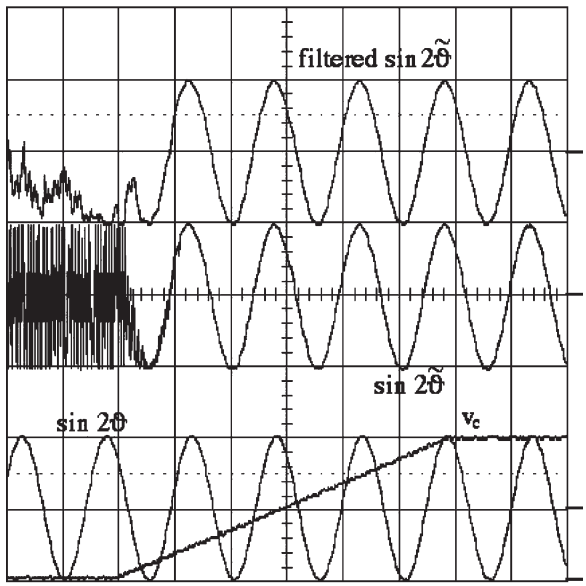

Fig. 13. Estimated angle $(\sin 2\tilde{\vartheta})$ for an injected carrier voltage v_c increased from 0 to 300 V ($i_d = 2$ A, $i_q = 10$ A). Exciting (rotating) voltage: v_c (150 V/div). Time base: 100 ms/div.

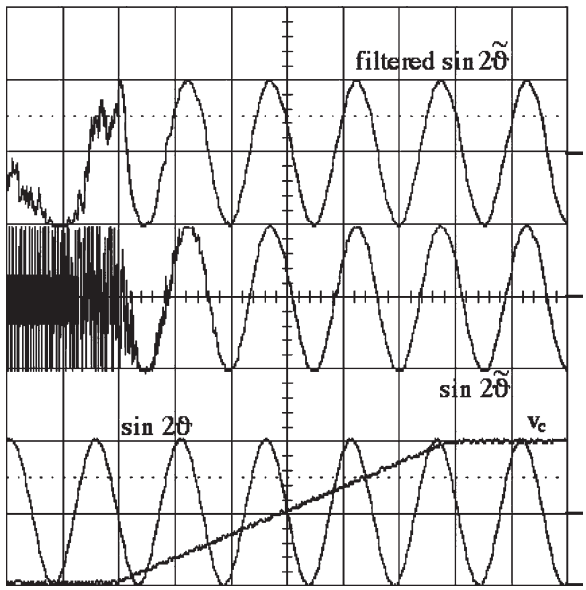

Fig. 14. Estimated angle $(\sin 2\tilde{\vartheta})$ for an injected carrier voltage v_c increased from 0 to 300 V ($i_d = 7$ A, $i_q = 20$ A). Exciting (rotating) voltage: v_c (150 V/div). Time base: 100 ms/div.

($i_d = 4, i_q = 0$) is set: this point looks the most critical in Fig. 9 and the situation is here confirmed. On the other hand, Fig. 12 shows that a small q-axis current ($i_d = 4$, $i_q = 2$) is sufficient to sensibly improve the behavior of the ($i_d = 4$, $i_q = 0$) point, as predicted by Fig. 9.

Last, Figs. 13 and 14 show two situations where the anisotropy is good and the angle estimation is well performed, even for reasonably low values of the voltage amplitude. The best performance looks that of Fig. 13, corresponding to the larger ar value (Fig. 9). Anyway, Fig. 14 shows a good behavior, corresponding to an overload situation, since the rated current is 10 A (peak). In conclusion, the impact of the equivalent anisotropy ratio ar is confirmed by experiment.

Fig. 9 also shows that reasonably good ar values are found in the area above the maximum Nm/A locus, that is for the working points of best practical interest, at load. Of course, at no load, a minimum i_d (or λ_d) value must be set. This value should be chosen in order to maximize the ar ratio, thus avoiding the most critical points.

From above, some considerations can be drawn concerning the most suited type and amplitude of a voltage excitation to be used in a practical implementation. As a trivial strategy, a rotating-voltage vector of quite large amplitude may be used. As an example, at a 400-Hz carrier frequency, a 100-V amplitude would correspond to 0.04 Vs, that is to nearly 4% of the rated flux, for the considered motor. However, the q-axis

injected current would rise, in the worst case, beyond 1 A (Fig. 3), which represents 10% of the rated current.

A reduction of the carrier frequency would reduce the voltage amplitude, but it is in contrast with the needed spectral separation between the fundamental ad carrier frequencies. Moreover, if constant-power operation were required beyond the base speed, the here considered ratio (8:1) between carrier and fundamental frequencies would be furtherly reduced, probably becoming insufficient for an effective filtering. In this case, the carrier frequency would be increased, leading to an even larger injected voltage, what is clearly unacceptable.

Of course, a proper optimization of the signal-to-noise ratio could minimize the needed voltage amplitude. Anyway, from the above example, two consequences of the general validity can be drawn. As a first consequence, injection of a pulsating voltage vector could be preferred, in this case, to the rotating one, which represents in general the suggested choice [23]. A reason is in the lower current amplitude at carrier frequency. Furthermore, the pulsating voltage is directed along the d-axis, while the motional EMF shows a phase displacement (from d-axis) between 90° and 135° (motoring). As a consequence, the two vectors never sum in phase, thus leading to a lower resultant voltage vector than in the rotating case.

As a second consequence, when a constant-power speed range is required, the voltage injection should be dropped-out before entering the flux-weakening range. This implies that a different sensorless approach has to be used, beyond a certain speed value: typically, an EMF-based approach can be valid, in this case. Of course, a smooth transition is welcome, up and down the chosen crossover speed.

In the following, an observer-based control scheme, which fulfils the above requirements, is shown and the obtained performance is verified by experiment.

IV. Sensorless Control Scheme

As a preliminary point, the choice is discussed of the control variables to be used. In general, i_d and i_q variables are directly controlled in ac motor drives, since they are measured variables. However, in the our case, the flux components λ_d, λ_q can be considered too, since the flux–current relationship (1) is practically of the algebraic type, at least if eddy currents are disregarded.

It was already shown by the authors [7], [10] that the best choice is the couple (λ_d, i_q), for many reasons. In fact, they represent the largest components of flux and current vectors, thus leading to low sensitivity to angular errors. This is especially useful during flux weakening at a high speed, when the i_d component can be very low. Moreover, the λ_d flux loop "sees" a linear system and a large bandwidth is obtainable. On the contrary, a i_d loop would have bandwidth problems, since its differential gain (l_d^{-1}) is much variable (Fig. 3). On the other hand, the i_q loop is maintained, since the torque is dominated by the $\lambda_d i_q$ term and a reasonably large bandwidth is anyway obtainable, in this case.

The used control scheme is shown in Fig. 15. A 125 V $\lambda_{\rm dc}$ sinusoidal oscillating flux is injected, at a 400-Hz frequency, owing to the large loop bandwidth: anyway some time leading

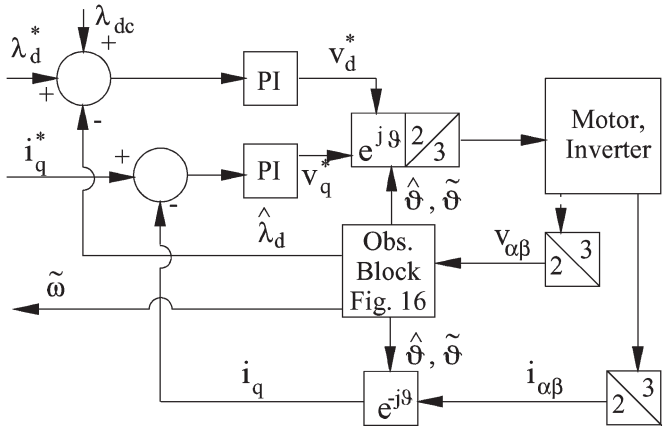

Fig. 15. Machine control structure.

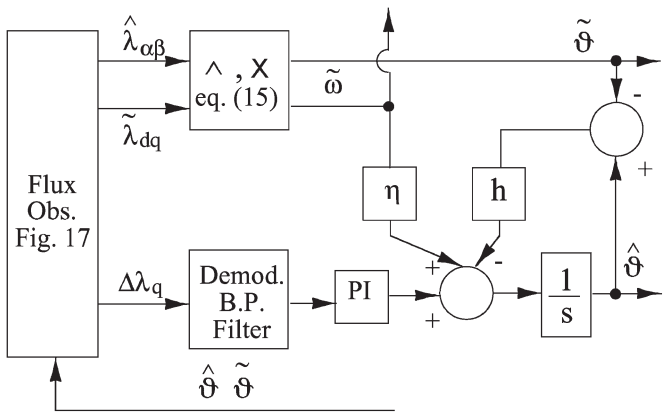

Fig. 16. Observer block.

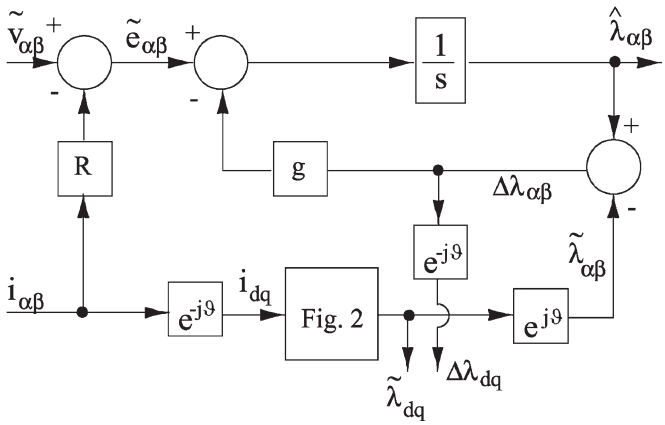

Fig. 17. Flux observer.

is still set. The $\lambda_{\rm dc}$ signal is dropped-out before reaching the voltage limit. The observer block in Fig. 15 is shown in Fig. 16, including the flux observer of Fig. 17.

The sensorless control scheme of Figs. 16 and 17 has been already illustrated by the authors in a previous paper [22]. Synthetically, the flux observer behaves as (15) shows, following at low frequency the estimate $\tilde{\lambda}_{\alpha\beta}$, based on Fig. 2 model, while voltage integration prevails, at high frequency

$$\hat{\lambda}_{\alpha\beta} = \frac{s}{s+g}\left(\frac{v_{\alpha\beta} - Ri_{\alpha\beta}}{s}\right) + \frac{g}{s+g}\tilde{\lambda}_{\alpha\beta}. \qquad (15)$$

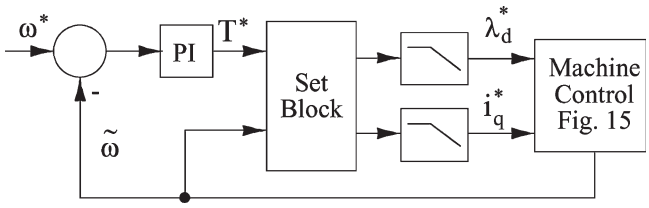

Fig. 18. Drive control scheme.

The choice of the crossover pulsation g is mainly affected by the quality of the voltage estimate $\tilde{v}_{\alpha\beta}$, which fails at a low frequency for the well-known reasons, chiefly the inverter's nonidealities. They could be someway compensated and the crossover shifted towards lower frequencies. We did not face this point, in the actual implementation. Also, the gain g could be made speed dependent, for stability considerations.

If the observed angle $\hat{\vartheta}$ is correct, the magnetic modeling of Fig. 2 allows calculation of the estimated flux $\tilde{\lambda}_{\alpha\beta}$ from the measured current $i_{\alpha\beta}$. The cross-saturation effect previously analyzed is then overcome and a zero q-axis component is produced by the d-axis-directed carrier flux $\lambda_{\rm dc}$. If, on the other hand, an alignment error $\hat{\vartheta} - \vartheta$ exists, some q-flux component arises, at the carrier frequency, and an alignment error can be generated to the tracking loop shown in Fig. 16. The $\Delta\lambda_q$ signal has been chosen at that aim, since it is inherently high-pass filtered, as

$$\Delta\lambda_{\alpha\beta} = \frac{s}{s+g}\left(\lambda_{\alpha\beta} - \tilde{\lambda}_{\alpha\beta}\right) \quad \lambda_{\alpha\beta} = \frac{v_{\alpha\beta} - Ri_{\alpha\beta}}{s}. \tag{16}$$

At high frequency, the $\hat{\lambda}_{\alpha\beta}$ observed flux mainly comes from a voltage integration, while tends to $\tilde{\lambda}_{\alpha\beta}$ at low frequency. As a consequence, an angle estimate $\tilde{\vartheta}$ is obtainable, for not too small frequencies, as

$$\sin\tilde{\vartheta} = \frac{\tilde{\lambda}_{dq} \wedge \hat{\lambda}_{\alpha\beta}}{\lambda^2} \quad \cos\tilde{\vartheta} = \frac{\tilde{\lambda}_{dq} \times \hat{\lambda}_{\alpha\beta}}{\lambda^2}. \tag{17}$$

In Fig. 16 this $\tilde{\vartheta}$ estimate is used, to supply the transformation matrices instead of the $\hat{\vartheta}$ signal when the carrier signal is dropped out, beyond a certain speed. A pole h is inserted between $\tilde{\vartheta}$ and $\hat{\vartheta}$, for smooth transition and noise filtering.

In Fig. 16, an estimated speed $\tilde{\omega}$ is also partially $(\eta < 1)$ injected to the tracking loop, to improve its dynamics. This $\tilde{\omega}$ speed is output to close the speed loop, as shown in Fig. 18. The set block in this figure performs several jobs:

1) share of torque demand between the set flux and current, in order to maximize the N·m/A ratio: anyway, a minimum flux value is set;
2) limitation of the set flux at high speed, to implement the flux-weakening profile; and
3) limitation of the set current to a maximum value at low speed and following the flux-weakening profile at high speed.

Low-pass filters (150 Hz) have been inserted, to slow down the required flux and current dynamics during fast transients: this proved to be opportune for sensorless operation. The bandwidth of the i_q loop was set to 350 Hz (average), while that of λ_d loop was 1.6 kHz. The obtained speed bandwidth was nearly 10 Hz, in the constant-torque speed range.

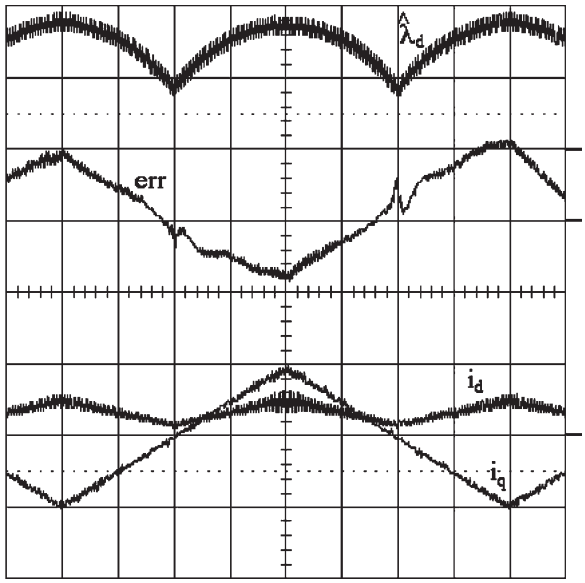

Fig. 19. Angular error with triangular set i_q current at standstill (cross-saturation effects dropped out from the flux observer). Observed flux: $\hat{\lambda}_d$ (0.5 Vs/div), measured error (15° el/div), motor currents: i_d, i_q (10 A/div). Time base 500 ms/div.

V. Experimental Results

In the following, some experimental results are given, showing the performance of the above described control structure. The adopted TLSyR motor is the same as in Section III (Fig. 3), whose flux–current characteristics are reported in Fig. 2. This motor is built in a standard induction-motor frame, self-cooled, as usual for general-purpose application. It is 18 N·m, 7 Arms rated, at 1500 r/min. The TLSyR motor is supplied by a 10-kHz switched insulated gate bipolar transistor (IGBT) inverter.

In Figs. 19 and 20, the motor is at standstill zero-speed controlled by the coaxial drive. A triangular i_q current is set, ± 10 A wide, while the corresponding i_d and λ_d values refer to the maximum N·m/A curve. The error between observed $\hat{\vartheta}$ and measured ϑ angles is shown too. In Fig. 19, the cross-saturation effect has been dropped out from the flux observer of Fig. 17: Thus, the Fig. 2 model has been reduced to $\lambda_d(i_d, 0)$ and $\lambda_q(0, i_q)$ curves only. As can be seen, it results in a quite large estimation error, corresponding to that predicted by Fig. 5. On the contrary, Fig. 20 shows a quite reduced error, since the cross-saturation is now included in the flux observer. This represents a further experimental confirmation of the impact of this phenomenon on sensorless control.

Both Figs. 21 and 22 refer to a situation where the cross-saturation is compensated and the motor runs at different speed values. The estimation error is shown together with the control variables, λ_d and i_q. At 100 r/min (Fig. 21) the quite low-estimation error can be appreciated ($\pm 4°$ ripple, mainly at no load). The injected $\lambda_{\rm dc}$ carrier signal can be outlined. Fig. 22 refers to a speed (1500 r/min) beyond the one at which the carrier is dropped out. The error looks limited also in this case,

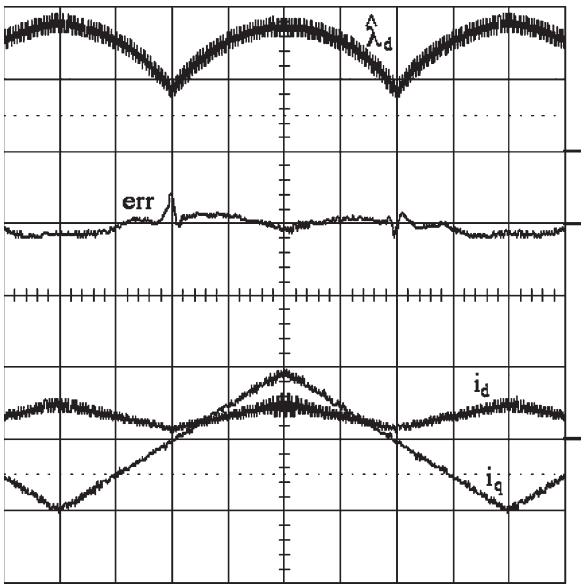

Fig. 20. Angular error with triangular set i_q current at standstill (cross-saturation effects included in the flux observer). Observed flux: $\hat{\lambda}_d$ (0.5 Vs/div), measured error (15° el/div), motor currents: i_d, i_q (10 A/div). Time base 500 ms/div.

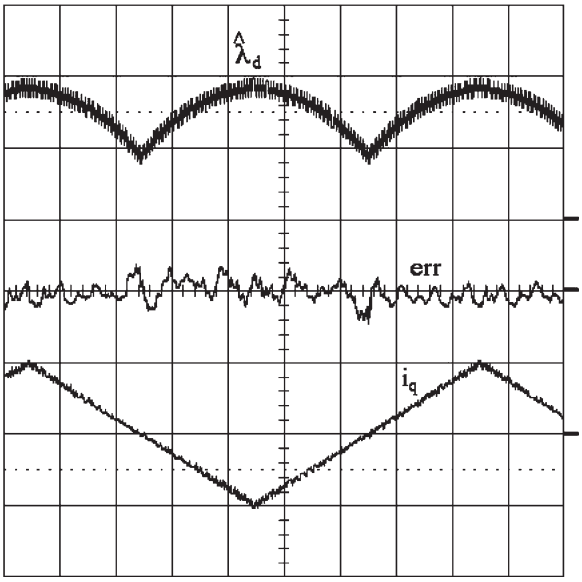

Fig. 21. Angular error with triangular set i_q current—100 r/min. Observed flux: $\hat{\lambda}_d$ (0.5 Vs/div), measured error: err (10° el/div), motor current: i_q (10 A/div). Time base 500 ms/div.

although some oscillations arise at no load, due to underdamped behavior of the EMF-based estimate. Let us also observe that the λ_d flux does not increase at high speed, because of the set voltage limitation.

In Figs. 23 and 24, step transients are shown, from 0 to 2000 r/min (Fig. 23) and vice versa (Fig. 24). Estimated speed $\tilde{\omega}$, λ_d flux, i_q current, and angular error are shown. As seen, the error is reasonably limited, also during fast transients. The obtained acceleration is 4000 rad/s^2, with a near-rated current. The motor inertia is 4.5×10^{-3} kg $\cdot$ m^2. The λ_d flux is reduced to nearly 50%, both at low speed (no load) and at high speed

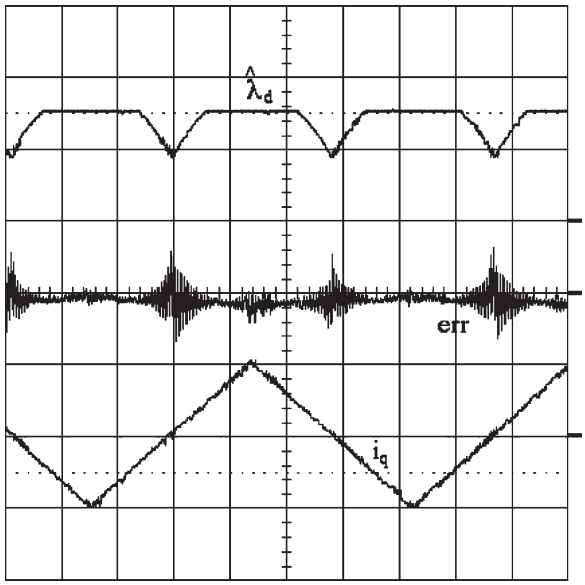

Fig. 22. Angular error with triangular set i_q current—1500 r/min. Observed flux: $\hat{\lambda}_d$ (0.5 Vs/div), measured error: err (10° el/div., motor current: i_q (10 A/div). Time base 500 ms/div.

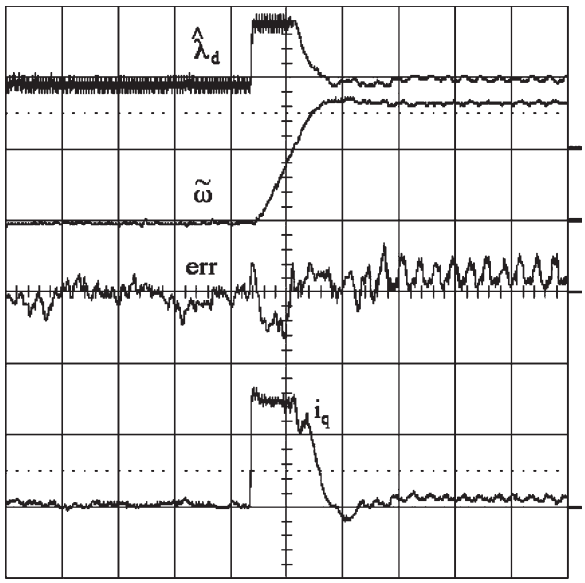

Fig. 23. Step speed transient (from zero up to 2000 r/min). Observed flux: $\hat{\lambda}_d$ (0.5 Vs/div), estimated speed $\tilde{\omega}$ (1250 r/min/div), measured error: err (10° el/div), motor current: i_q (5 A/div). Time base 50 ms/div.

(voltage limitation). The speed below which the carrier signal is injected can be appreciated (near to 1000 r/min).

In Fig. 25, a triangular speed is set, $\pm$1000 r/min at a 10-Hz frequency. The corresponding i_q current is near to the rated value, that is 8.8 A. The quite good dynamics can be appreciated, still with limited angular errors. Last, Fig. 26 shows a sinusoidal speed response, pointing out the near to 10-Hz bandwidth. Both set and estimated speeds are shown, in this case.

The above shown behavior looks satisfactory, for a sensorless control. Anyway, it could be improved, by compensating the inverter's nonidealities and someway damping the flux-observer behavior at high speed.

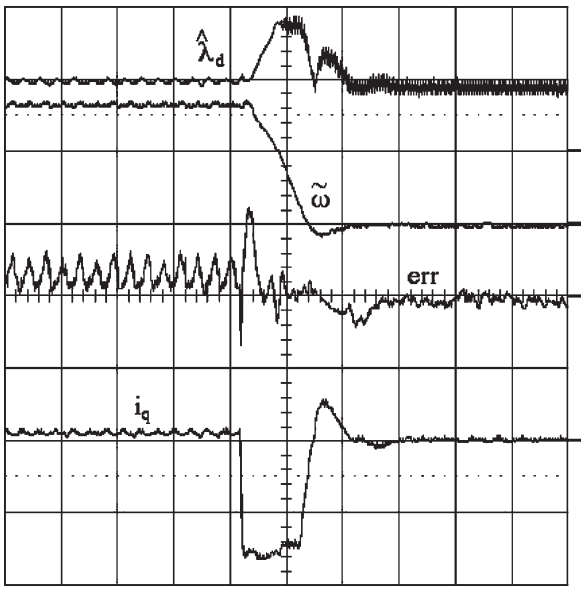

Fig. 24. Step speed transient (from 2000 r/min down to zero). Observed flux: $\hat{\lambda}_d$ (0.5 Vs/div), estimated speed $\tilde{\omega}$ (1250 r/min/div), measured error: err (10° el/div), motor current: i_q (5 A/div). Time base 50 ms/div.

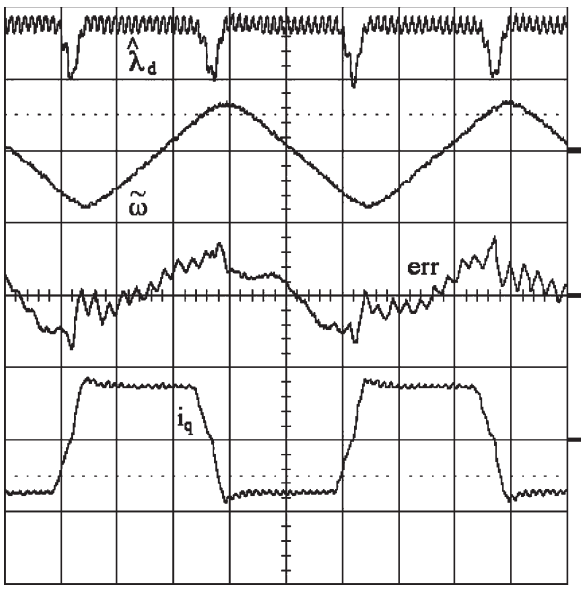

Fig. 25. Triangular set speed. Observed flux: $\hat{\lambda}_d$ (0.5 Vs/div), estimated speed $\tilde{\omega}$ (1250 r/min/div), measured error: err (10° el/div), motor current: i_q (10 A/div). Time base 20 ms/div.

VI. Conclusion

The strong impact of the cross-saturation on a sensorless control of the TLSyR motors has been proven by experiment. It cannot be disregarded, if an effective control is wanted. Compensation of the cross-saturation effect requires a detailed knowledge of the magnetic behavior of the machine, which must be carefully identified. If this knowledge is introduced in a flux-observer scheme, the standard performance of the (i_d, i_q)-based control schemes can be sensibly improved, in particular when a constant-power speed range is present.

The obtained sensorless drive performance is suited to a low-accuracy position control and to those speed controls where very high accuracy of speed is wanted. This performance, together with the acceptable dynamics and the inherent low-cost of the motor, makes this kind of drive particularly suited to general-purpose applications.

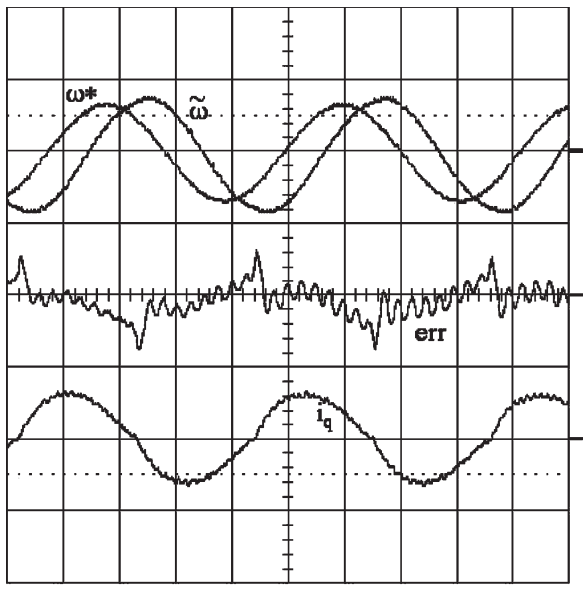

Fig. 26. Sinusoidal set speed. Speed reference: ω^* (500 r/min/div), estimated speed $\tilde{\omega}$ (500 r/min/div), measured error: err (10° el/div), motor current: i_q (10 A/div). Time base 20 ms/div.

References

[1] M. Schroedl and P. Weinmeier, "Sensorless control of reluctance machines at arbitrary operating conditions including standstill," *IEEE Trans. Power Electron.*, vol. 9, no. 2, pp. 225–231, Mar. 1994.

[2] P. L. Jansen and R. D. Lorenz, "Transducerless position and velocity estimation in induction and salient AC machines," *IEEE Trans. Ind. Appl.*, vol. 31, no. 2, pp. 240–247, Mar./Apr. 1995.

[3] J. Holtz, "State of the art of controlled AC drives without speed sensor," in *Proc. Int. Conf. Power Electron. Drive Syst.*, 1995, vol. 1, pp. 1–6.

[4] *Sensorless Control of AC Motor Drives: Speed and Position Sensorless Operation*, K. Rajashekara, A. Kawamura, and K. Matsuse, Eds. New York: IEEE Press, 1996.

[5] F. Blaschke, J. Van der Burgt, and A. Vandenput, "Sensorless direct field orientation at zero flux frequency," in *Proc. IEEE-IAS Annu. Meeting*, San Diego, CA, Oct. 7–10, 1996, vol. 1, pp. 189–196.

[6] M. Schroedl, "Sensorless control of AC machines at low speed and standstill based on the "INFORM" method," in *Proc. IEEE-IAS Annu. Meeting*, San Diego, CA, Oct. 7–10, 1996, vol. 1, pp. 270–277.

[7] A. Vagati, G. Franceschini, and M. Pastorelli, "High performance control of synchronous reluctance motor," *IEEE Trans. Ind. Appl.*, vol. 33, no. 4, pp. 983–991, Jul./Aug. 1997.

[8] P. Vas, *Sensorless Vector and Direct Torque Control*, vol. xxxi. New York: Oxford Univ. Press, 1998, p. 729 .

[9] A. Vagati, M. Pastorelli, G. Franceschini, and C. Petrache, "Design of low-torque-ripple synchronous reluctance motors," *IEEE Trans. Ind. Appl.*, vol. 34, no. 4, pp. 758–765, Jul./Aug. 1998.

[10] A. Vagati, M. Pastorelli, G. Franceschini, and V. Drogoreanu, "Flux-observer-based high-performance control of synchronous reluctance motors by including cross saturation," *IEEE Trans. Ind. Appl.*, vol. 35, no. 3, pp. 597–605, May/Jun. 1999.

[11] S. Ogasawara and H. Akagi, "Implementation and position control performance of a position-sensorless IPM motor drive system based on magnetic saliency," *IEEE Trans. Ind. Appl.*, vol. 34, no. 4, pp. 806–812, Jul./Aug. 1998.

[12] S.-J. Kang, J.-I. Ha, and S.-K. Sul, "Position controlled synchronous reluctance motor without rotational transducer," in *Proc. IEEE 33rd IAS Annu. Meeting*, 1998, vol. 1, pp. 671–676.

[13] M. J. Corley and R. D. Lorenz, "Rotor position and velocity estimation for a salient-pole permanent magnet synchronous machine at standstill and high speeds," *IEEE Trans. Ind. Appl.*, vol. 34, no. 4, pp. 784–789, Jul./Aug. 1998.
[14] M. D. Manjrekar, T. A. Lipo, S. C. G. Chang, and K. S. Kim, "Flux tracking methods for direct field orientation," in *Proc. ICEM*, Istanbul, Turkey, Sep. 1998, pp. 1022–1029.
[15] J. Holtz, "Sensorless position control of induction motors—An emerging technology," *IEEE Trans. Ind. Electron.*, vol. 45, no. 6, pp. 840–851, Dec. 1998.
[16] J. I. Ha and S. K. Sul, "Sensorless field orientation control of an induction machine by high frequency signal injection," *IEEE Trans. Ind. Appl.*, vol. 35, no. 1, pp. 45–51, Jan./Feb. 1999.
[17] A. Consoli, F. Russo, G. Scarcella, and A. Testa, "Low and zero speed sensorless control of synchronous reluctance motors," *IEEE Trans. Ind. Appl.*, vol. 35, no. 5, pp. 1050–1057, Sep./Oct. 1999.
[18] M. W. Degner and R. D. Lorenz, "Position estimation in induction machines utilizing rotor bar slot harmonics and carrier-frequency signal injection," *IEEE Trans. Ind. Appl.*, vol. 36, no. 3, pp. 736–742, May/Jun. 2000.
[19] A. Vagati, M. Pastorelli, F. Scapino, and G. Franceschini, "Impact of cross saturation in synchronous reluctance motors of the transverse-laminated type," *IEEE Trans. Ind. Appl.*, vol. 36, no. 4, pp. 1039–1046, Jul./Aug. 2000.
[20] A. Vagati, A. Canova, M. Chiampi, M. Pastorelli, and M. Repetto, "Design refinement of synchronous reluctance motors through finite-element analysis," *IEEE Trans. Ind. Appl.*, vol. 36, no. 4, pp. 1094–1102, Jul./Aug. 2000.
[21] A. Consoli, G. Scarcella, G. Tutino, and A. Testa, "Sensorless field oriented control using common mode currents," in *Proc. IEEE-IAS Annu. Meeting*, Roma, Italy, Oct. 8–12, 2000, pp. 1866–1873.
[22] A. Vagati, M. Pastorelli, P. Guglielmi, and E. Capecchi, "Position sensorless control of transverse-laminated synchronous reluctance motors," *IEEE Trans. Ind. Appl.*, vol. 36, no. 3, pp. 736–742, May/Jun. 2001.
[23] R. D. Lorenz, "Practical issues and research opportunity when implementing zero-speed sensorless control," in *Proc. 5th ICEMS*, Aug. 18–20, 2001, vol. 1, pp. 1–10.
[24] J. Holtz, "Sensorless control of induction motor drives," *Proc. IEEE*, vol. 90, no. 8, pp. 1359–1394, Aug. 2002.
[25] A. Vagati, P. Guglielmi, M. Pastorelli, and G. Pellegrino, "Position-sensorless control of permanent-magnet-assisted synchronous reluctance motor," *IEEE Trans. Ind. Appl.*, vol. 40, no. 2, pp. 615–622, Mar./Apr. 2004.

Paolo Guglielmi was born in Imperia, Italy, in 1970. He received the M.Sc. degree in electronic engineering and the Ph.D. degree in electrical engineering from the Politecnico di Torino, Turin, Italy, in 1996 and 2001, respectively.

In 1997, he joined the Dipartimento di Ingegneria Elettrica, Politecnico di Torino, where he became a Researcher in 2002. His fields of interest are power electronics, high-performance servo drives, and computer-aided design of electrical machines. He has authored several papers published in technical journals and conference proceedings.

Dr. Guglielmi is a Registered Professional Engineer in Italy.

Michele Pastorelli (M'05) was born in Novara, Italy, in 1962. He received the Laurea and Ph.D. degrees in electrical engineering from the Politecnico di Torino, Turin, Italy, in 1987 and 1992, respectively.

In 1988, he joined the Dipartimento di Ingegneria Elettrica, Politecnico di Torino, where he is currently an Associate Professor. His fields of interest include power electronics, high-performance servo drives, and energetic behaviors of electrical machines. He has authored about 70 papers published in technical journals and conference proceedings.

Dr. Pastorelli is a Registered Professional Engineer in Italy.

Alfredo Vagati (M'88–SM'92–F'98) received the Laurea degree in electrical engineering from the Politecnico di Torino, Turin, Italy, in 1970.

After a few years working in industry with Olivetti, he joined the Politecnico di Torino, in 1975 as Assistant Professor. From 1982 to 1990, he was an Associate Professor of Electrical Drives. In 1990, he became a Professor of Electrical Machines and Drives at the University of Cagliari, Italy. In 1991, he rejoined the Politecnico di Torino in the same capacity. He chaired the Department of Electrical Engineering of the Politecnico di Torino from 1995 to 2003. His scientific activity, in the field of electrical machines and drives, has focused mainly on high-performance ac drives. He has been involved in several industrial projects in the field of ac drives, as both a designer and a scientific reference. His most important activity concerns design and control of newly developed, high-performance synchronous reluctance (SyR) motors. He has led several countrywide and European research projects in the field of design and control of synchronous-machine-based drives for different applications including home appliances and the automotive world. He has authored or coauthored more than 90 technical papers.

Prof. Vagati is a permanent member of the Technical Program Committee of the Power Conversion and Intelligent Motion (PCIM) International Conference and Exhibition. He is also a member of the Industrial Drives and the Electric Machines Committees of the IEEE Industry Applications Society.